Measuring the concentration of freestream species on a hypersonic transpiration-cooled stagnation point

Marc Ewenz Rocher *, Tobias Hermann † and Matthew McGilvray ‡
The University of Oxford, Department of Engineering, Osney Mead, The Southwell Building,
Oxford OX2 0ES, United Kingdom

Madeleine Grossman § and Luc Vandeperre ¶
Imperial College London, Department of Materials & Centre for Advanced Structural Ceramics,
London SW7 2AZ, United Kingdom

This paper presents direct surface concentration measurements of a transpiration cooled stagnation point in hypersonic flow. Pressure sensitive paint (PSP) is employed on a porous alumina sample to measure the concentration of freestream species and thus how well the coolant mitigates mass diffusion from the freestream to the surface. Experiments are conducted at Mach 6.9 at three different Pitot pressures: 10 kPa, 20 kPa and 30 kPa. Porous alumina is chosen due to its ability to bond PSP and its similar microstructure to porous Ultra-High-Temperature Ceramics. Nitrogen, Argon and Krypton are used as injection gases at mass flow rates ranging from 0.01 - 0.55 kg/m^{2}s, in order to displace up to 99% of the freestream gas at the surface. The experimental data shows that transpiration cooling is more effective in displacing freestream gas than predicted by analytical models and numerical solutions. The microheterogeneous surface with recessed pores means there is an additional pressure gradient within the first layer of pores.

Nomenclature

B_m = $\frac{F}{St_{m0}}$, blowing parameter for mass transfer
C_2 = empirical constant, m^2/s
$D_{i,j}$ = diffusion coefficient for species i into species j, m^2/s
D_k = Knudsen diffusivity, m^2/s
f = function of
F = $\frac{\dot{m}_{\text{inj}}}{\rho_\infty u_\infty}$, blowing ratio
I = PSP intensity, counts

---

[*] DPhil Candidate, Oxford Thermofluids Institute, University of Oxford, AIAA Member.

[†] Departmental Lecturer, Oxford Thermofluids Institute, University of Oxford, AIAA Member.

[‡] Associate Professor, Oxford Thermofluids Institute, University of Oxford, AIAA Member.

[§] Post-doctoral Research Assistant, Imperial College London.

[¶] Professor of Structural Ceramics, Imperial College London.

J = bulk mole flux, mol/m^{2}s

J_i = mole flux of species i, mol/m^{2}s

K_D = Darcy coefficient, m^2

K_F = Forchheimer coefficient, m

K_m = mass transfer coefficient, m/s

$\dot{m}$ = mass flux, kg/m^{2}s

M = Mach number

n = mole density

p_0 = freestream total pressure, Pa

p = pressure, Pa

R = effective nose radius, m

$\mathcal{R}$ = universal gas constant, J/mol K

Sc = $\frac{\mu}{\rho D}$, Schmidt number

St_m = $\frac{K_m}{u_\infty}$, mass transfer Stanton number

T = temperature, K

T_0 = total temperature, K

u = velocity, m/s

$\frac{du_e}{dx}$ = velocity gradient, 1/s

W = molecular weight, g/mol

x = mass fraction

y = mole fraction

z = material depth

β = molecular slip factor

λ = scaling factor

μ = viscosity, Pa s

ρ = density, kg/m^3

Subscripts

0 = no blowing

c = coolant

e = boundary layer edge

ext = external gas

fginj = foreign gas injection

inj = injected gas

noinj = no injection

ref = reference condition

w = wall

∞ = freestream

I. Introduction

Hypersonic flight incurs high heat fluxes requiring a thermal protection system (TPS) to protect the crew and payload. Stagnation points, leading edges on slender bodies and scramjet intakes have extreme heat fluxes and heat loads due to their small radii, which are designed to minimize aerodynamic drag. This results in elevated surface temperatures over the duration of the flight path. Thermally and chemically protecting these key vehicle components is crucial to extending the flight envelope.

The most common TPS is an ablative, as used in many hypervelocity re-entry vehicles, such as the Hayabusa capsule [1]. Transpiration cooling is a potential shape-stable TPS in which a coolant is fed through a porous wall, forming a protective film upon exiting [2]. Although both technologies eject gas, pyrolisis products and a coolant, respectively, their performance is limited by oxidation and surface recombination. This is because oxygen, both molecular and atomic, diffuses to the material, degrading [3] and heating [4] the surface, respectively. Charred ablative surfaces recess due to oxidation and nitration [5], while transpiration cooling materials oxidize up to 2500 K below their melting temperature [6–8]. Predicting the oxidation behavior is vital to improve the performance of these protection systems.

Oxidation is driven by high temperatures, but also by the oxygen partial pressure at the surface [9]. Thus, the oxygen concentration at a stagnation point with mass injection needs to be predicted. This can be achieved numerically using the self-similar laminar boundary layer equations [10] or a full CFD solver. Alternatively it can be found using a semi-analytical correlation [11], which is reviewed in section II.

These methods have not been validated experimentally due to the lack of data. This work aims to provide the first experimental measurements of oxygen concentration at a stagnation point with blowing. While oxidation is caused by atomic oxygen in some real-flight trajectories, the present study focuses on molecular oxygen diffusion only. This is due to the temperature limitations imposed by the experimental facilities and diagnostics. The concentration of molecular oxygen at the wall is measured directly using a novel pressure sensitive paint diagnostic [12] on a flat faced hemispherical probe in the Oxford High Density Tunnel. A range of freestream conditions, coolant gases and blowing ratios are explored and compared to the analytical solution described in the next section.

II. Analytical Correlation

When modeling the mass transfer of freestream oxygen to the wall, it is desirable to non-dimensionalise the characteristic quantities. Ref. [11] showed analytically and numerically that the mass transfer reduction is related to the mass blowing parameter $B_m = \frac{F}{St_{m0}}$, which is the blowing ratio, normalised by the uncooled mass Stanton number. The blowing ratio denotes the ratio of coolant to freestream mass flux, $F = \frac{\rho_c u_c}{\rho_\infty u_\infty}$, while the uncooled Stanton number is defined as the uncooled mass transfer coefficient to the freestream velocity, $St_{m0} = \frac{K_{m0}}{u_\infty}$.

The mass Stanton number at the stagnation point in the absence of blowing was derived as [11]

$$St_{m0} = 0.89 \frac{\rho_e}{\rho_w} \frac{\mu_e}{\sqrt{\rho_w \mu_w}} \sqrt{\frac{du_e}{dx} \frac{1}{u_\infty}}, \tag{1}$$

where $\frac{du_e}{dx}$ is the velocity gradient at the boundary layer edge. The blowing parameter is related to the mass Stanton number ratio as follows:

$$\frac{St_m}{St_{m0}} = \frac{\lambda B_m}{e^{\lambda B_m} - 1}, \tag{2}$$

where λ is a weighting factor defined as

$$\lambda = \left(\frac{\mu_e T_w}{\mu_w T_e}\right)^{0.5} Sc_w^{0.6} 2.52 \frac{\rho_e}{\rho_w} \times \left(\frac{W_{\text{ext}} D_{\text{ext;ext}}}{W D_{\text{inj;ext}}}\right)_w^{0.75}. \tag{3}$$

The reduction in the ratio of mass Stanton numbers is directly related to the mass fraction of coolant at the wall, $x_{c,w}$:

$$\frac{St_m}{St_{m0}} = 1 - x_{c,w}, \tag{4}$$

which can be obtained experimentally by the pressure sensitive paint diagnostic used in this work.

III. Experimental Setup

The experiments were conducted on the stagnation probe model shown in Figure 1, featuring a 25 mm radius hemispherical probehead. The nose of the probehead was machined off creating a 21 mm diameter flat face with a 16 mm diameter hole in its center. A flat, 5mm thick porous sample is glued in centrally from the back using Deluxe Materials AD68 Speed Epoxy II, which also acts as sealant. Kapton tape kept the front and back surface clean and was stripped off after the epoxy had cured. Then, a pressure sensitive paint solution consisting of 0.1 mmol $\left[\mathrm{Ru}\left(\mathrm{dpp}_3\right)\right]^{2+}$ luminophores suspended in 200 ml Dichloromethane, was applied with an air brush. More details on the PSP and the application method can be found in [12]. The rest of the hemisphere was also spray painted with PSP, after being primed with an ISSI fast response porous underlayer. The PSP coated probehead can be seen in Fig 3. Note that the layer is so thin, that the orange hue of the luminophores is barely visible.

The alumina samples with 39% porosity were produced by the Centre for Advanced Structural Ceramics at Imperial College London and used in all tests. Materials typically used in transpiration cooling, such as UHTCs [7], C/C composites [13], stainless steel and bronze [14] do not bond PSP, creating the need for a representative material. Alumina particles with a diameter of 6.45 μm were sintered for 3 hours at 1700°C. More details and images of the surface microstructure can be found in [12], where the same material is used. The geometry consisted of a 2 mm thick, 14 mm diameter disk on top of a 3 mm thick, 20 mm diameter disk. The sample was sintered in a mold with the correct diameters, but made slightly thicker and polished down afterwards. This allowed precise control over the thickness and opened the pores at the surface. A subsequent ultrasonic bath removed any dust and lose particles clogging the pores.

The pressure and temperature in the pressurized plenum behind the sample were measured by an XT-190M-35bara Kulite and an Omega 5TC-TT-KI-40-1M fast response thermocouple, respectively. The Kulite has an accuracy of ± 3.5 kPa and the thermocouple of ± 2.2 K or ± 0.75%, whichever is greater. A National Instruments PXIe-8135 controller equipped with a PXIe-6368 (2 MHz/channel) card recorded the pressure and temperature data at 200 kHz.

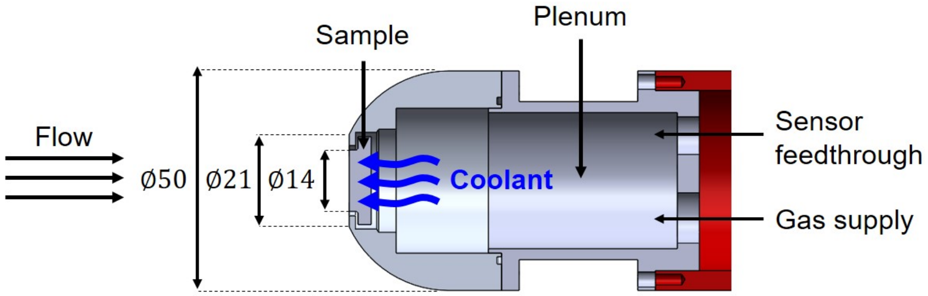

Fig. 1 Annotated section view of the experimental model.

A schematic of the optical setup is shown in Fig. 2. A Luminus PT-120-B-L11-EPG with a dominant wavelength of 460 nm illuminated the PSP. The LED intensity varies with temperature, but an in-built thermistor was used to calibrate this effect and account for it in the post-processing step [12]. A mirror next to the nozzle exit reflects the luminescence of the sample into the Photron Fastcam Mini AX 200 900K high speed camera, which is equipped with a 550 nm long pass filter to block scattered blue light from the LED. The camera was operated at a 2000 Hz frame rate, 0.5 ms shutter speed, 512 x 512 pixel resolution and a bit depth of 12 bit. It was equipped with a Tamron SP AF 70-200mm F/2.8 Di LD (IF) macro telephoto zoom lens, enabling it to capture 256 x 256 pixels on the probehead and 50 x 50 pixels on the sample. For calibration of the PSP, the static pressure in the test section was measured by an Inficon Sky CDG025D 100 torr gauge with an accuracy of 0.2% of the reading.

The permeability of the sample was measured pre- and post-experiment according to the procedure detailed in [15].

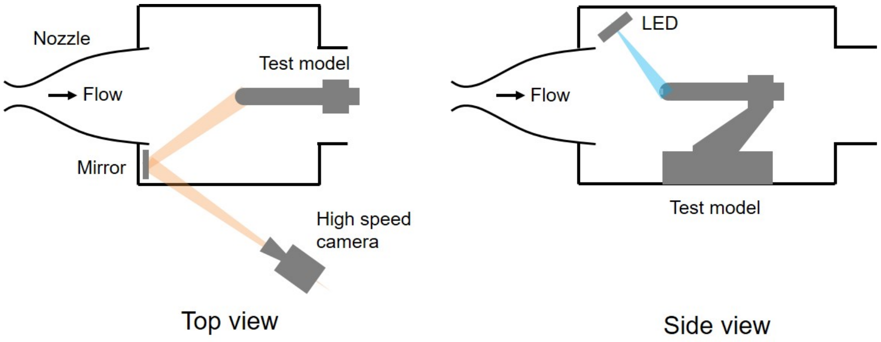

Fig. 2 Schematic of the optical setup.

As the plenum pressure increased from 0 to 20 bar, the mass flux was recorded by an Omega FMA5518A mass flow controller with an accuracy of ± 0.05 slpm. The Darcy and Forchheimer coefficients are K_D = 3.04 $\times 10^{-15}$ m^2 and K_F = 1.16 $\times 10^{-9}$ m, respectively.

The outflow distribution of the employed porous injector is characterized by hot-wire anemometry with air injection and no cross-flow. The air remained isothermal, at room temperature, throughout the sample. The measurements were taken by a Dantec Dynamics 55P11 hot wire with the following dimensions: 5 μm in diameter and 1.25 mm in length. More details on this technique can be found in [15]. The outflow is extremely uniform, between 0.008 - 0.012 m/s. Note that the outflow velocity is very similar to the bulk velocity at 4 bar differential pressure of 0.009 m/s, predicted by the Darcy-Forchheimer equation.

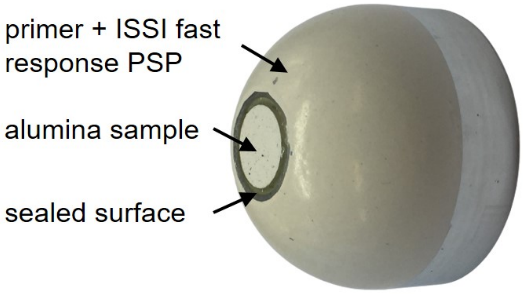

Fig. 3 Post-campaign photograph of the porous alumina glued into the probehead.

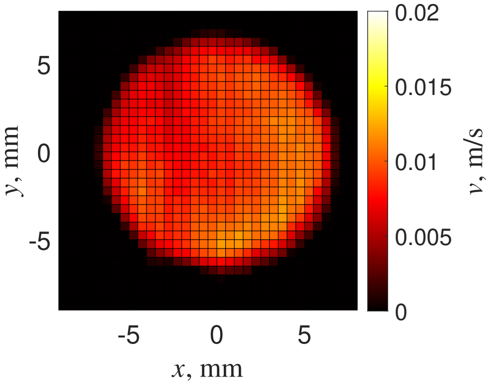

Fig. 4 Velocity map of the sample at 4 bar differential pressure and no cross flow.

The experiments were conducted in the Oxford High Density Tunnel at Mach 6.9. More details on this facility can be found in [16]. A new feature developed prior to this experimental campaign is the use of pure nitrogen in the freestream. The stagnation temperature and Pitot pressures are summarised in Table 1. The injection parameters are shown in Table 2, while Tables 3 and 4 summarize the wall, freestream and diffusion parameters. Note that the velocity gradient for a perfect hemisphere is given as $\frac{du_e}{dx} = \frac{1}{R}\sqrt{\frac{2(p_e - p_\infty)}{\rho_e}}$. The effective radius for the flat faced hemisphere used in this work is R = 43.9 mm and was obtained using CFD.

Table 1 Overview of test conditions.

Condition	Injectant	p_0	T_0	p_∞	T_∞	p_e	T_e	ρ_e	μ_e	$St_{m0} \times 10^3$
		[kPa]	[K]	[kPa]	[K]	[kPa]	[K]	$[\frac{\mathrm{kg}}{\mathrm{m}^3}]$	[Pa.s]	[-]
1	N_2	612	436	0.162	41.7	10	436	0.08	2.32×10^{-5}	1.17
2	N_2	1224	436	0.324	41.7	20	436	0.16	2.32×10^{-5}	0.82
3	N_2	1836	436	0.486	41.7	30	436	0.24	2.32×10^{-5}	0.67
4	Ar	612	436	0.162	41.7	10	436	0.08	2.32×10^{-5}	1.17
5	Kr	612	436	0.162	41.7	10	436	0.08	2.32×10^{-5}	1.17

Table 2 Injection parameters.

Condition	Injected mass flux $[\frac{\mathrm{kg}}{\mathrm{m}^2\mathrm{s}}]$	F [%]	λB_m [-]
1	0.017, 0.074, 0.197, 0.232, 0.310	0.143, 0.637, 1.658, 1.959, 2.623	0.281, 1.245, 3.315, 3.912, 5.229
2	0.107, 0.278, 0.445	0.443, 1.151, 1.847	1.275, 3.318, 5.310
3	0.135, 0.346, 0.546	0.374, 0.957, 1.507	1.319, 3.366, 5.313
4	0.014, 0.072, 0.226, 0.279, 0.371	0.120, 0.609, 1.914, 2.237, 3.138	0.226, 1.047, 3.061, 3.747, 4.957
5	0.009, 0.044, 0.094	0.076, 0.370, 0.801	0.123, 0.534, 1.080

Table 3 Wall and freestream parameters for all experiments.

T_w	μ_w	Sc_w	M	u_∞	$\frac{du_e}{dx}$
[K]	[Pa.s]	[-]	[-]	$[\frac{\mathrm{m}}{\mathrm{s}}]$	$[\frac{1}{\mathrm{s}}]$
295	1.73×10^{-5}	0.7812	6.9	891	11300

Table 4 Molar mass and binary diffusion coefficients at p_e = 10 kPa.

W_air	W_{N_2}	W_Ar	W_Kr	$D_\mathrm{air;air}$	$D_\mathrm{Ar;air}$	$D_\mathrm{Kr;air}$
$[\frac{\mathrm{g}}{\mathrm{mol}}]$	$[\frac{\mathrm{g}}{\mathrm{mol}}]$	$[\frac{\mathrm{g}}{\mathrm{mol}}]$	$[\frac{\mathrm{g}}{\mathrm{mol}}]$	$[\frac{\mathrm{m}^2}{s}]$	$[\frac{\mathrm{m}^2}{s}]$	$[\frac{\mathrm{m}^2}{s}]$
28.97	28	40	83.8	2.02×10^{-4}	1.92×10^{-4}	1.51×10^{-4}

IV. PSP Post-Processing

The raw image recorded by the camera is depicted in Fig. 5. It shows the photon count per pixel, where the dark current has already been subtracted. Due to the 550 nm long pass filter only the PSP luminescence is captured. The frames are averaged over the steady-state test period. All frames are normalized by the reference intensity I_ref recorded just before starting the wind tunnel, with its corresponding reference pressure, p_ref. The normalized intensity signal $\frac{I_\mathrm{ref}}{I}$

is then spatially averaged over the region of interest marked in red in Fig. 5. This provides further noise reduction and improves the signal quality.

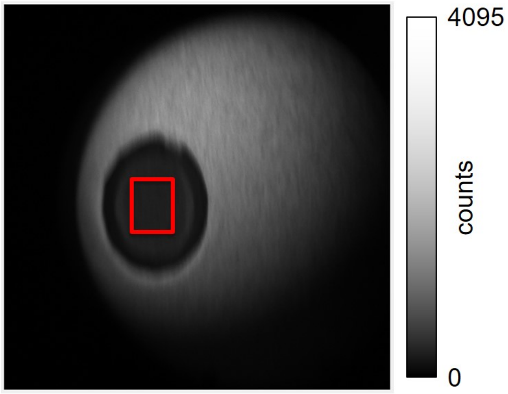

Fig. 5 Raw image of PSP luminescence with region of interest marked in red.

A. Temperature effects

Pressure sensitive paint is also sensitive to temperature: $I = f(p, T)$. Thermal effects need to be removed from the PSP signal, before it is converted into pressure. For this purpose, every air freestream shot was coupled with a N_2 freestream shot. When an oxygen-deficient gas, such as N_2, Kr or Ar is injected into a N_2 crossflow, all changes in the PSP signal will be due to temperature effects only, $I = f(p_{\text{ref}}, T)$. This thermal PSP trace, $\frac{I(p_{\text{ref}},T)}{I(p_{\text{ref}},T_{\text{ref}})}$, is used to extract the pure pressure signal from the respective air freestream shots, assuming that the thermal properties of air and N_2 are similar. Even though the shots were recorded across 2 weeks, they exhibit a good repeatability. The pure pressure signal is extracted by normalizing the air-freestream data (second term on the RHS) by the respective nitrogen-freestream intensity (first term on the RHS):

$$\frac{I(p_{\text{ref}}, T_{\text{ref}})}{I(p, T_{\text{ref}})} = \frac{I(p_{\text{ref}}, T)}{I(p_{\text{ref}}, T_{\text{ref}})} \frac{I(p_{\text{ref}}, T_{\text{ref}})}{I(p, T)} \tag{5}$$

The pure pressure signal, $\frac{I(p_{\text{ref}},T_{\text{ref}})}{I(p,T_{\text{ref}})}$, can be converted to pressure using a calibration curve, which is described in the following.

B. Obtaining the calibration curve

In theory PSP is described by the Stern-Volmer equation

$$\frac{I(p_{\text{ref}}, T_{\text{ref}})}{I(p, T_{\text{ref}})} = A(T_{\text{ref}}) + B(T_{\text{ref}}) \left(\frac{p}{p_{\text{ref}}}\right), \tag{6}$$

where A and B are the Stern-Volmer coefficients. However, in practice PSP behaves highly non-linearly and it is therefore more practical to express the relationship between intensity and pressure as:

$$p = C\left(\left(\frac{I\left(p_{\mathrm{ref}}, T_{\mathrm{ref}}\right)}{I\left(p, T_{\mathrm{ref}}\right)}\right)^{D} - 1\right) \tag{7}$$

where the fitting parameters C and D were obtained in-situ before the experiment at room temperature with no crossflow. The intensity is recorded from vacuum to atmospheric pressure. Each intensity measurement is plotted against the corresponding pressure reading. The fitting parameters are found to be $C = 7.383 \pm 0.040$ and $D = 3.728 \pm 0.011$. A new calibration curve was obtained every day to account for changes in room temperature and photodegradation. The oxygen partial pressure for every experiment was obtained by removing the temperature effects, using Eq. (5) and then applying Eq. (7).

V. Results and Discussion

The aim of this experiment is to measure the coolant concentration on a transpiration cooled surface. The quantity measured by the PSP is the partial pressure of oxygen, p_{O_2}. Because the injected gases are oxygen-free, p_{O_2} is directly related to the partial pressure of freestream air, p_{air} via the mole fraction of O_2 in air:

$$p_{\mathrm{air}} = \frac{p_{O_2}}{y_{O_2;\mathrm{air}}}. \tag{8}$$

Due to the binary nature of the mixture, the coolant partial pressure is simply the difference between the boundary layer edge pressure and the air partial pressure, $p_c = p_e - p_{\mathrm{air}}$. The injection does not affect the pressure field at the stagnation point. Thus, the boundary layer edge pressure is the pressure measured by the PSP in the no-injection case, $p_e = p_{\mathrm{air;noinj}}$. The mole fraction of the coolant during injection thus becomes

$$p_c = p_{\mathrm{air;noinj}} - p_{\mathrm{air;fginj}} \tag{9}$$

$$y_c = 1 - \frac{p_{\mathrm{air;fginj}}}{p_{\mathrm{air;noinj}}} = 1 - \frac{p_{O_2;\mathrm{fginj}}}{p_{O_2;\mathrm{noinj}}}, \tag{10}$$

where the subscript fginj denotes foreign gas injection. The mass fraction of coolant is the product of its mole fraction and molar mass divided by the average molar mass:

$$x_c = \frac{y_c W_c}{y_c W_c + y_{\mathrm{air}} W_{\mathrm{air}}} \tag{11}$$

$$= \frac{y_c W_c}{y_c W_c + \left(1 - y_c\right) W_{\mathrm{air}}}. \tag{12}$$

The coolant concentration is recovered by multiplying the mass fraction, by the density at the wall, $\rho_w = \frac{p_e}{RT_w}$. The pressure is known from the uncooled case and the molar mass required for the gas constant is a function of the known mass fraction. The fluid wall temperature is assumed to be equal to the solid wall temperature, which was calculated using the Porous Impulse Response Analysis for Transpiration cooling Evaluation (PIRATE) code [17]. It was found to rise by less than 5 K for the uncooled cases and less than 3K for the cooled cases. These values were used in the uncertainty analysis to quantify the error of ρ_w.

Figure 6 shows the mass fraction of air at the surface against the blowing ratio for all conditions. A trend can be observed, whereby increasing blowing ratios reduce the mass fraction of freestream air at the wall. As expected, the data points do not collapse, indicating that the blowing ratio alone is not sufficient to characterize the displacement of freestream gas at the surface. Furthermore there is no quantitative correlation relating the blowing ratio F to the air mass fraction.

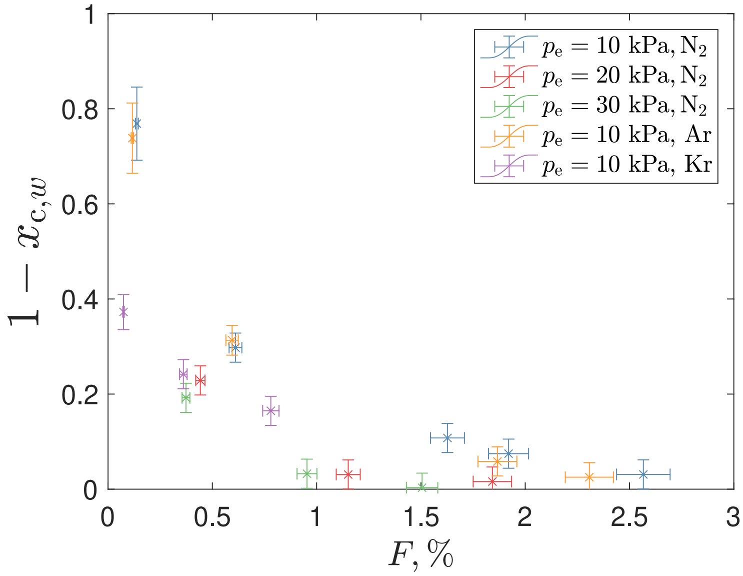

Fig. 6 Mass fraction of air at the wall vs blowing ratio for all conditions.

Figure 7 presents the same data, but now plotted against the analytically obtained, scaled mass blowing parameter, λB_m. While the data generally follows the trend and is reasonably close to the analytical solution, a greater reduction in freestream mass transfer is seen than predicted by the theory. It is theorized that the reduced oxygen concentration compared to theory is due to the porous interface effect. When the PSP particles are spray painted onto the porous surface, they are evenly distributed across the irregular surface. This means that some fly inside the pores, as schematically depicted in Fig. 8. As the channels are small and the mass flux high, there still exists a pressure gradient during injection [12]. The numerically derived correlation, which is represented by the black line in Fig. 7 only model the diffusion through the boundary layer up to the surface of the material, marked by the dotted line in Fig. 8. However, in the

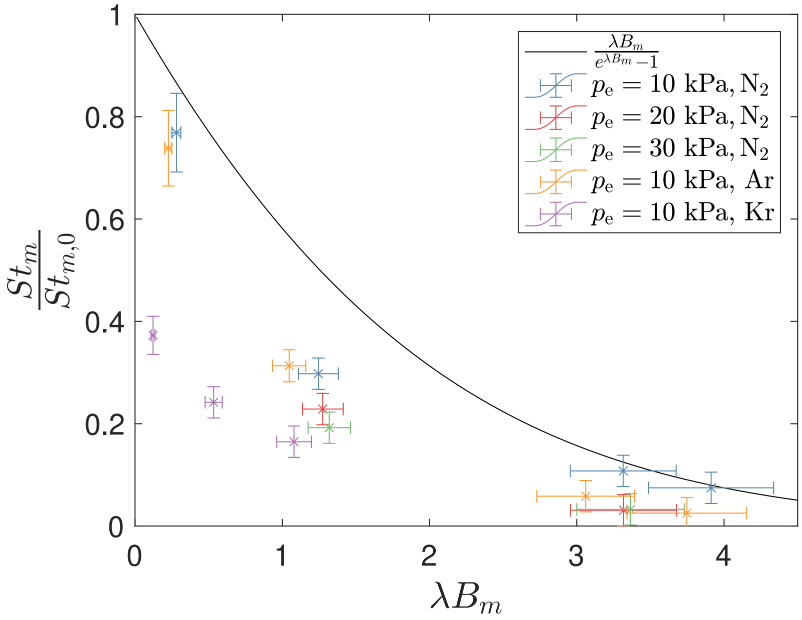

(a) Linear

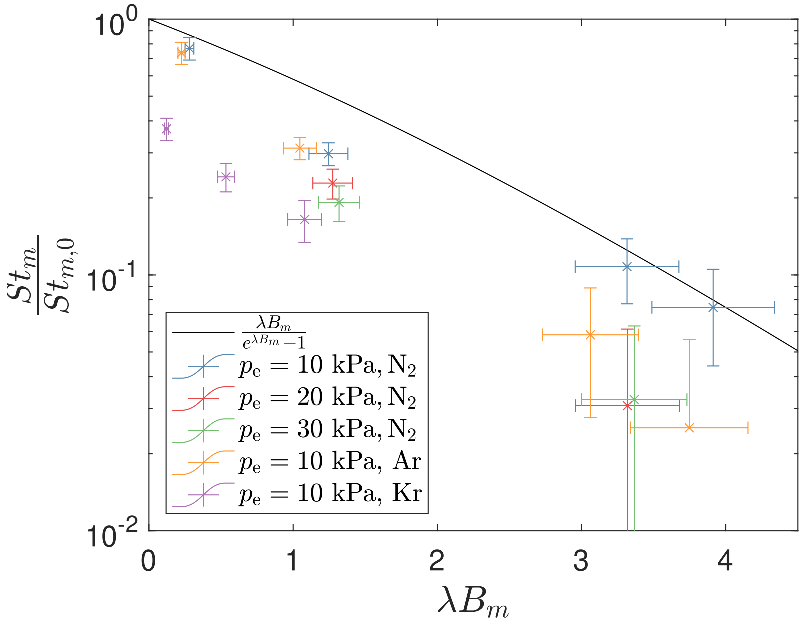

(a) Semi-logarithmic

Fig. 7 Stanton number reduction vs blowing parameter for all conditions.

experiment, the oxygen molecules need to additionally overcome an adverse pressure gradient to reach the luminophores inside the pores. Numerical simulations usually assume a perfectly flat and homogeneous wall, neglecting this porous interface effect [10]. They will therefore produce a conservative estimate of the mass Stanton number reduction, which is useful for initial design work. Further investigation is required to understand whether the PSP distribution is uniform

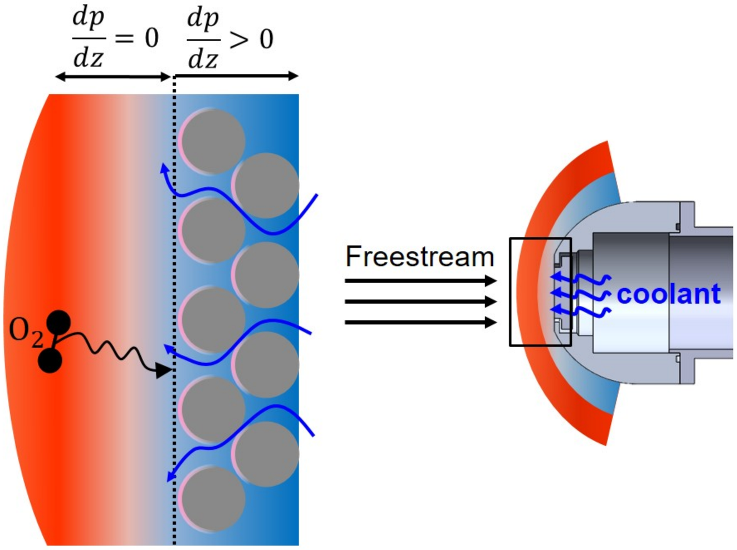

Fig. 8 Schematic of the PSP distribution and pressure gradient on the porous interface.

across the material surface and therefore whether their luminescence can be taken as the average luminescence of the interface. Since the calibration curve is linear up to about 10 kPa, this would yield the average O_2 partial pressure on the real, microheterogeneous boundary of the porous material.

The experimental data for conditions 2 and 3, illustrated in Fig. 7, shows an even larger discrepancy to the theoretical prediction than condition 1. The freestream pressure was doubled and tripled, while the mass flow rate was increased by 41% and 73%, respectively. According to the theoretical prediction and CFD simulations, this should yield the same $\frac{St_m}{St_{m0}}$ reduction as for condition 1. However, as the mass flux and therefore the pressure gradient across the material increases, the porous interface effect is accentuated and even less luminophores are reached by the freestream gas. The Argon data follows the same trend as the nitrogen results, while the Krypton results deviate from the theoretical prediction the most. Krypton appears to be much more effective in displacing oxygen than anticipated. An analytical model for the diffusion against a pressure gradient is needed to explain these observations.

A. Diffusion against a pressure gradient

The effect of a pressure gradient on the gaseous diffusion in porous media was first quantified in Ref. [18]. The analysis starts with the species continuity equation:

$$J_1 = -n \left(D_1\right)_{\text{eff}} \left(\frac{dy_1}{dz}\right) + y_1 J \delta_1 \tag{13}$$

where the first term describes diffusion and the second advection. The parameter $n = \frac{p}{\mathcal{R}T}$ is the mole density. $(D_1)_{\text{eff}}$ is an effective diffusion coefficient defined as

$$\frac{1}{(D_1)_{\text{eff}}} = \frac{1}{(D_{12})_{\text{eff}}} + \frac{1}{(D_{1\text{k}})} \tag{14}$$

where D_{1k} is the Knudsen diffusivity and D_{12} the binary diffusion coefficient. The subscript eff denotes the effective diffusion coefficient, which takes into account the tortuosity of the porous medium. For the small material depths studied in this work, it is assumed to be equal to the normal diffusion coefficient.

The factor δ_1 is zero for Knudsen diffusion and unity for normal diffusion and is defined as follows:

$$\frac{1}{\delta_1} = 1 + \frac{(D_{12})_{\text{eff}}}{D_{1k}} = \frac{(D_{12})_{\text{eff}}}{(D_1)_{\text{eff}}}, \tag{15}$$

where D_{1k} is the Knudsen diffusivity. The pores of the material used in this study were small enough for Knudsen diffusion to be significant. For $T_w = 295$ K, $p_e = 10$ kPa, a collision diameter for air of 3.617 Å and a pore diameter of 2 μm, the Knudsen number is 0.35. J denotes the bulk flow of molecules and is defined by the forced flow equation

$$J = \beta J_1 - \left(\frac{C_2}{kT}\right)\frac{dp}{dz} \tag{16}$$

where the first term represents the molecular slip and the second term accounts for a mole flux due to a pressure gradient across the porous material. In the absence of a pressure gradient, a bulk flow of molecules can still exist if the particles on either side of the porous medium have different molar masses. The lighter molecules diffuse quicker thereby creating a net flux towards the heavy molecules. The slip term $\beta = 1 - \sqrt{\frac{W_1}{W_2}}$ relates this molecular slip to the molar mass. The second term in Eq. (16) strongly resembles the Darcy term of the Darcy-Forchheimer equation [15]. In fact, it is the mole flux due to a pressure gradient which can be obtained from Table 2, dividing the mass flux by the average molar mass of molecules. Inserting Eq. (16) into Eq. (13) one obtains

$$J_1 = -nD_1\left(\frac{dy_1}{dz}\right) + y_1\left(\beta J_1 - \frac{\dot{m}}{\bar{W}}\right)\delta_1 \tag{17}$$

$$J_1\left(1 - \beta y_1 \delta_1\right) = -nD_1\left(\frac{dy_1}{dz}\right) - y_1\frac{\dot{m}}{\bar{W}}\delta_1 \tag{18}$$

Assuming that no air enters the plenum and thus that the diffusive and advective molar fluxes balance each other out throughout the porous medium, one can set the net molar flux J_1 to zero and obtains

$$nD_1 \left(\frac{dy_1}{dz} \right) = -y_1 \frac{\dot{m}}{\bar{W}} \delta_1 \tag{19}$$

$$nD_1 \left(\frac{dy_1}{dz} \right) = -y_1 \frac{\dot{m}}{\bar{W}} \frac{D_1}{D_{12}} \tag{20}$$

$$nD_{12} \left(\frac{dy_1}{dz} \right) = -y_1 \frac{\dot{m}}{\bar{W}} \tag{21}$$

The term nD_{12} is constant throughout the porous material because the pressure terms in the molar density and the diffusivity cancel each other out. Thus, one can integrate the partial differential equation and use the known mole fraction of air at the surface to obtain

$$y_{\mathrm{air}}\left(z\right) = y_{\mathrm{air};w} e^{\frac{\mathcal{R}T_w}{p_e D_{\mathrm{air;inj}}} \frac{\dot{m}}{\bar{W}} z} \tag{22}$$

In this calculation, it was assumed that the mole fraction of air at the surface, $y_{\mathrm{air};w}$, was that predicted by the semi-analytical correlation [11]. It can be seen from Eq. (22) that for a constant wall temperature, the porous diffusion is only a function of the mass flow rate and the injectant parameters, which affect the average molar mass and the diffusion coefficient. Figure 9 (a) illustrates how an increase in mass flux causes a larger relative reduction in air mass fraction inside the pores. This can also be observed in Figure 7. The three data points with edge pressures of 10, 20 and 30 kPa at a λB_m of about 1.27 all have the same numerically predicted air mass fraction. However, due to increasing mass fluxes (Table 2) from the 10 kPa through to the 30 kPa case, lower mass fractions are expected (Eq. (22)), despite having the same λB_m.

The effect of injectant properties on the diffusion of air into the pores is less obvious. A heavier gas, such as Krypton will reduce the molar flux $\frac{\dot{m}}{\bar{W}}$ in Eq. (22) and this will lead to a higher mole fraction of air for a given mass flow rate. However, when taking into account the change in diffusion coefficient and the conversion from mole to mass fraction of air (Eq. (12)), Krypton is more effective at displacing freestream gas if the mass fraction of air at the surface is high. If the mass fraction of air at the surface is low then the reduction in mole flux outweighs the conversion from mole to mass flux and Krypton becomes less effective. This effect is depicted in Fig. 9 (b). One can see in Fig. 7 that Krypton is much more effective than nitrogen at high mass fractions of air at the wall, corresponding to low λB_m values. Argon, however, has a similar effectiveness as nitrogen.

The effective depth is the distance to which the predicted oxygen which reaches the porous interface (dotted line in Fig. 8) has to diffuse into the pores to match the experiment.

The marker in Figure 10 (a) shows the effective depth for the low blowing case of condition 1. The relative error in the large blowing cases was too high to make a sensible calculation. Figure 10 (b) depicts the effective depth for all low blowing conditions. One can see that it is approximately 0.1 - 1 μm, which matches the order of the pore size of the porous medium of 2μm. It is stressed that the prediction of the effective pore depth is simply an approximation to understand whether this could be a physical effect and it should not be considered to be a quantitative model. The mass flux deeper inside the pores will be higher due to the area ratio and a detailed direct numerical simulation would be required to model this effect.

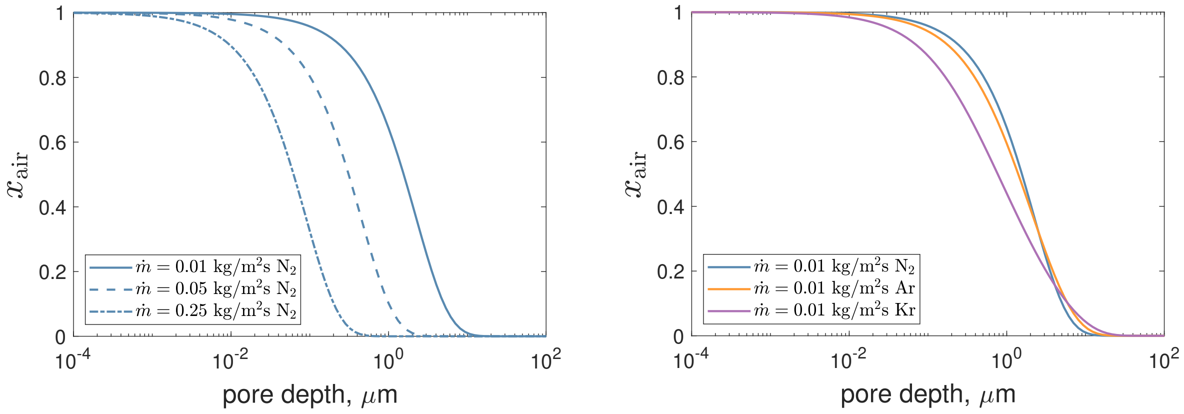

(a) Effect of mass flux (b) Effect of injectant

Fig. 9 Diffusion of freestream gas into a pore with mass injection.

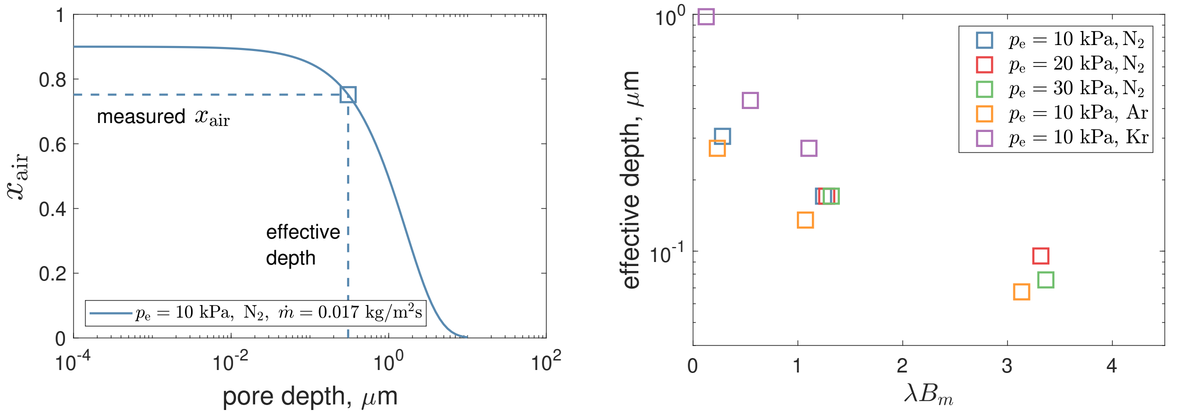

(a) Calculation of effective depth (b) Effective depth for all low blowing conditions

Fig. 10 Effective depth of PSP molecules inside the pores.

VI. Conclusion

The concentration of freestream species on a hypersonic stagnation point with mass injection was measured experimentally for the first time. The experimental data follows the theoretical trends well, but shows higher oxidation protection than predicted. This is because of the irregular porous surface. Numerical models assume that the porous surface is perfectly flat, but in reality it also has pores. The freestream air needs to overcome an adverse pressure gradient to reach the projected surface. This effect is not taken into account by the models, which is why they underpredict the oxygen protection provided by mass injection. The analytical models with a flat surface assumption will remain extremely useful for a conservative estimate of freestream gas at the surface. However, they could be improved in the future using the experimental data presented in this work to take into account the microheterogeneity of the porous surface.

Funding Sources

This research is funded by the EPSRC grant ”Transpiration Cooling Systems for Jet Engine Turbines and Hypersonic Flight” (reference: EP/P000878/1).

Acknowledgments

The authors of this paper would like to thank Greg King for his dedication and assistance in instrumenting the experimental rig, as well as Luke Doherty and Maïlys Buquet for the operation of the High Density Tunnel. The authors would like to extend their gratitude to Jack Hillyer and Eric Hembling for measuring the core flow diameter and Pitot pressure profiles.

References

[1] Uyanna, O., and Najafi, H., “Thermal protection systems for space vehicles: A review on technology development, current challenges and future prospects,” *Acta Astronautica*, Vol. 176, 2020, pp. 341–356. https://doi.org/10.1016/j.actaastro.2020.06.047.

[2] Böhrk, H., Elsäßer, H., and Weihs, H., “Flight Data from the Faceted TPS on SHEFEX II,” *8th European Symposium on Aerothermodynamics for Space Vehicles*, ESA Conference Bureau Noordwijk, The Netherlands, 2015, p. 1.

[3] Ewenz Rocher, M., McGilvray, M., Hermann, T. A., Ifti, H. S., Hufgard, F., Eberhart, M. F., Meindl, A., Loehle, S., Giovannini, T., and Vandeperre, L. J., “Testing a transpiration cooled zirconium-di-boride sample in the plasma tunnel at IRS,” *AIAA Scitech 2019 Forum*, 2019, p. 1552. https://doi.org/10.2514/6.2019-1552.

[4] Otsu, H., Fujita, K., and Ito, T., “Application of the Transpiration Cooling Method for Reentry Vehicles,” *Collection of Technical Papers - 45th AIAA Aerospace Sciences Meeting*, Vol. 21, 2007. https://doi.org/10.2514/6.2007-1209.

[5] Lachaud, J., van Eekelen, T., Scoggins, J. B., Magin, T. E., and Mansour, N. N., “Detailed chemical equilibrium model for porous ablative materials,” *International Journal of Heat and Mass Transfer*, Vol. 90, 2015, pp. 1034–1045. https://doi.org/10.1016/j.ijheatmasstransfer.2015.05.106.

[6] Hermann, T., McGilvray, M., and Naved, I., “Performance of Transpiration-Cooled Heat Shields for Reentry Vehicles,” *AIAA Journal*, Vol. 58, No. 2, 2020, pp. 830–841. https://doi.org/10.2514/1.J058515.

[7] Loehman, R., Corral, E., Dumm, H. P., Kotula, P., Tandon, R., et al., "Ultrahigh-Temperature Ceramics For Hypersonic Vehicle Applications." *Industrial Heating*, Vol. 71, No. 1, 2004, pp. 36–38. https://doi.org/10.2172/887260.

[8] Bacos, M., "Carbon-carbon composites: oxidation behavior and coatings protection," *Le Journal de Physique IV*, Vol. 3, No. C7, 1993, pp. C7–1895. https://doi.org/10.1051/jp4:19937303.

[9] Parthasarathy, T., Rapp, R., M. Opeka, M., and Kerans, R., "A model for the oxidation of ZrB2, HfB2 and TiB2," *Acta Materialia*, Vol. 55, 2007, pp. 5999–6010. https://doi.org/10.1016/j.actamat.2007.07.027.

[10] Steinheuer, J., "Berechnung der laminaren Zweistoff-Grenzschicht in der hypersonischen Staupunktströmung mit temperaturabhängigen Stoffbeiwerten," *ZAMM-Journal of Applied Mathematics and Mechanics/Zeitschrift für Angewandte Mathematik und Mechanik*, Vol. 51, No. 3, 1971, pp. 209–223. https://doi.org/10.1002/zamm.19710510308.

[11] Ewenz Rocher, M., Hermann, T., McGilvray, M., and Gollan, R., "Correlation for Species Concentration on a Hypersonic Stagnation Point with Mass Injection," *AIAA Journal*, 2021, pp. 1–12. https://doi.org/10.2514/1.J061159.

[12] Ewenz Rocher, M., Hermann, T., McGilvray, M., Ifti, H. S., Vieira, J., Hambidge, C., Quinn, M. K., Grossman, M., and Vandeperre, L., "Pressure-sensitive paint diagnostic to measure species concentration on transpiration-cooled walls," *Experiments in Fluids*, Vol. 63, No. 1, 2022, pp. 1–11. https://doi.org/10.1007/s00348-021-03355-9.

[13] Reimer, T., Kuhn, M., Gülhan, A., Esser, B., Sippel, M., and van Foreest, A., "Transpiration cooling tests of porous CMC in hypersonic flow," *17th AIAA International Space Planes and Hypersonic Systems and Technologies Conference*, 2011, p. 2251. https://doi.org/10.2514/6.2011-2251.

[14] Liu, Y.-Q., Jiang, P.-X., Xiong, Y.-B., and Wang, Y.-P., "Experimental and numerical investigation of transpiration cooling for sintered porous flat plates," *Applied Thermal Engineering*, Vol. 50, No. 1, 2013, pp. 997–1007. https://doi.org/10.1016/j.applthermaleng.2012.08.028.

[15] Ifti, H. S., Hermann, T., and McGilvray, M., "Flow characterisation of transpiring porous media for hypersonic vehicles," *22nd AIAA International Space Planes and Hypersonics Systems and Technologies Conference*, 2018, p. 5167. https://doi.org/10.2514/6.2018-5167.

[16] McGilvray, M., Doherty, L. J., Neely, A. J., Pearce, R., and Ireland, P., "The Oxford High Density Tunnel," *20th AIAA International Space Planes and Hypersonic Systems and Technologies Conference*, 2015, p. 3548. https://doi.org/10.2514/6.2015-3548.

[17] Hermann, T., Naved, I., and McGilvray, M., "Tool for Rapid Transient Transpiration-Cooled Reentry Simulation," *AIAA Journal*, Vol. 58, No. 2, 2020, pp. 842–853. https://doi.org/10.2514/1.J058516.

[18] Evans III, R., Watson, G., and Mason, E., "Gaseous diffusion in porous media. II. Effect of pressure gradients," *The Journal of Chemical Physics*, Vol. 36, No. 7, 1962, pp. 1894–1902. https://doi.org/10.1063/1.1701287.

A. Uncertainty analysis

The blowing parameter scales linearly with the mass flux, thus accurately measuring the mass flux is crucial. The permeability was measured twice, before and after the experimental campaign. The permeability decreased by 5% throughout the 3 week long test campaign. This could be due to a small leak in the experimental setup during the pre-campaign permeability measurement. Alternatively it may have been caused by freestream debris blocking the pores. The black particles can clearly be seen in Fig. 3. A conservative error of $\frac{\delta m_{\text{inj}}}{m_{\text{inj}}} = \pm 5\%$ was assumed in the results to account for these effects.

The second largest error source is the velocity gradient. The velocity gradient was assessed using CFD as the flat face did preclude the use of an analytical approximation for perfect hemispheres. The velocity gradient was found to be 11300 ± 300 1/s.

The boundary layer edge pressure and temperature were given an error of ±0.4 kPa and ±5 K, respectively. This amounts to 4% for a boundary layer edge pressure of 10 kPa and 1.1% for a temperature of 436 K. The freestream mass flux is defined as:

$$\dot{m}_e = \rho_e v_e = \frac{p_e}{RT_e} M_e \sqrt{\gamma R T_e} = \frac{p_e}{\sqrt{RT_e}} M_e \sqrt{\gamma}, \tag{23}$$

Thus, taking into account the errors of the pressure and temperature, the combined uncertainty becomes

$$\delta \dot{m}_e = \sqrt{\left(\frac{\partial \dot{m}_e}{\partial p_e}\delta p_e\right)^2 + \left(\frac{\partial \dot{m}_e}{\partial T_e}\delta T_e\right)^2} \tag{24}$$

yielding a relative error $\frac{\delta \dot{m}_e}{\dot{m}_e}$ of 4.04%

The same method is applied to chain the individual uncertainties together for the blowing ratio, $F = fn\left(\dot{m}_{\text{inj}}, \dot{m}_e\right)$. This yields an error of 6.4 %.

The camera has three error sources: shot noise, dark current and readout noise. The shot noise can be quantified by adding the total number of photon counts required for each data point in Fig. 7. Each CCD sensor counts between 600 - 1200 photons, depending on the setting. The lower bound of 600 will be used as a conservative value. As the data is spatially averaged by 39 x 29 pixels and then time averaged across 80 frames, the total counts for one data point are 600 x 39 x 29 x 80 = 54,288,000. Thus the signal to noise ratio is $\sqrt{54,288,000} = 7368$ and the 95% confidence interval for each measurement ±0.027%. The dark current was found to introduce a standard deviation of 20 counts. This leads to a 95% confidence interval of $\frac{\pm 2 \times 20}{600} = \pm 6.7\%$ per pixel and 0.022% for 29 x 39 x 80 pixels. A readout noise value of 41e- was provided by the manufacturer, which at a full well capacity of 16,000e- yields an error of approximately ±0.002%. Therefore, all camera error sources are deemed negligible.

The experiments were conducted in the span of two weeks. Daily calibrations were conducted as described in section IV.B to account for photodegradation, ambient temperature, humidity, drifts in the optical setup and any other environmental factors that may have affected the PSP response. Eleven calibration curves were produced which for a given intensity ratio $\frac{I_{\mathrm{ref}}}{I}$ output pressures with a spread of up to ±10%. The spread did not correlate with any of the above factors. Therefore a very conservative error of ± 10% or 300 Pa, whichever is greater, was applied in the post-processing to the PSP oxygen partial pressure signal.

The error bars shown in Fig. 7 account for all errors mentioned in this section.